Journal of Colloid and Interface Science 629 (2023) 111–120

Contents lists available at ScienceDirect

Journal of Colloid and Interface Science

journal homepage: www.elsevier.com/locate/jcis

Fine-tune *d*-band center of cobalt vanadium oxide nanosheets by *N*-doping as a robust overall water splitting electrocatalyst

Zuyang Luo [a], Qimin Peng [a], Zhiyang Huang [a], Lixia Wang [a], Yuting Yang [a], Jiaxin Dong [a,*], Tayirjan Taylor Isimjan [b,*], Xiulin Yang [a,*]

[a] Guangxi Key Laboratory of Low Carbon Energy Materials, School of Chemistry and Pharmaceutical Sciences, Guangxi Normal University, Guilin 541004, Guangxi, China
[b] Saudi Arabia Basic Industries Corporation (SABIC) at King Abdullah University of Science and Technology (KAUST), Thuwal 23955-6900, Saudi Arabia

HIGHLIGHTS

- A serial of *N*-doping cobalt vanadium oxide electrocatalysts were designed by two steps.
- Nitride temperature affects the microstructure, crystallinity and N doping content of the catalyst.
- *N*-doping cobalt vanadium oxides display excellent activity and stability for OER and HER.
- DFT calculations suggest that *N*-doping can fine-tune the *d*-band center and band gap to facilitate intermediate adsorption and electron motion.

GRAPHICAL ABSTRACT

A series of cobalt vanadium oxides were synthesized by feasible hydrothermal growth followed by nitridation at different temperatures. N-$Co_2V_2O_7$@NF (350 °C) and N-Co_2VO_4/VO_2@NF (400 °C) exhibited excellent OER and HER performance with overpotentials of 310 mV and 224 mV at 100 mA cm^{-2}, long-term stability for 170 h and 700 h at 100 mA cm^{-2}, and assembled as anode and cathode for robust overall water splitting (1.93 V, 500 mA cm^{-2}).

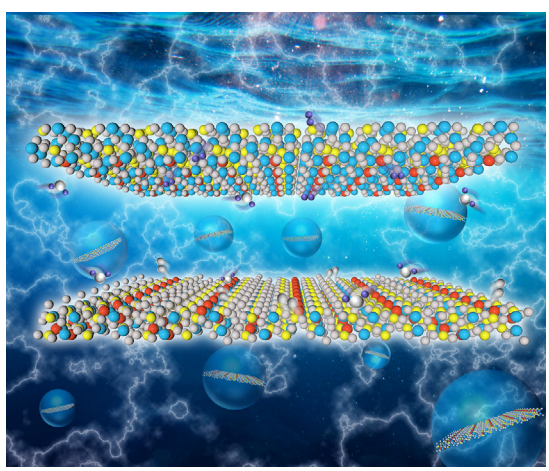

ARTICLE INFO

Article history:
Received 25 July 2022
Revised 5 September 2022
Accepted 12 September 2022
Available online 16 September 2022

Keywords:
Cobalt vanadium oxides
N-doping nanosheet
Conductivity
Overall water splitting
Theoretical calculation

ABSTRACT

Developing high-activity, long-durability, and noble metal-free oxygen evolution (OER) and hydrogen evolution (HER) cocatalysts are the bottlenecks for efficient overall water splitting (OWS). Here, novel cobalt vanadium oxides doped by nitrogen were synthesized by nitriding $Co_2V_2O_7$@NF precursor at 300–450 °C for OER and HER reactions. N-$Co_2V_2O_7$@NF (350 °C) and N-Co_2VO_4/VO_2@NF (400 °C) show remarkable OER and HER performance with overpotentials of 310 mV and 224 mV at high current density (100 mA cm^{-2}). Besides, they also revealed long-term solid stability even after 170 h and 700 h of continuous performance. Furthermore, the N-$Co_2V_2O_7$@$NF^{(+)}$||N-Co_2VO_4/VO_2@$NF^{(-)}$ OWS device possesses a cell voltage of 1.93 V at 500 mA cm^{-2} better than RuO_2@$NF^{(+)}$||Pt/C@$NF^{(-)}$ (2.02 V) and can operate for 60 h with almost no degradation. This extraordinary performance can be attributed to the nanosheet structure, which can maximize the exposure of active sites and accelerate the mass transfer. Moreover, density functional theory (DFT) calculations suggest that *N*-doping can fine-tune the d-band center

* Corresponding authors.
E-mail addresses: chemdjx@gxnu.edu.cn (J. Dong), isimjant@sabic.com (T.T. Isimjan), xlyang@gxnu.edu.cn (X. Yang).

https://doi.org/10.1016/j.jcis.2022.09.069

and band gap to facilitate intermediate adsorption and electron motion. The method presented here can be applied in other novel *N*-doped electrocatalysts for the energy field.

1. Introduction

As an alternative to conventional fossil fuels, electrochemical overall water splitting (OWS) is a viable method for producing green hydrogen [1]. However, the high overpotentials of oxygen and hydrogen evolution cocatalysts (OER and HER) limit the system efficiency [2]. RuO_2 and Pt/C are the most potent OER and HER catalysts reported so far, but their rarity and high-cost limit further utilization at the industrial scale [3]. Thus, it is of industrial significance to explore the OER and HER catalysts with low-cost, high-activity and long-term durability for water splitting.

Recently, abundant reserves of transition metal-based materials have been reported for OER and HER, including oxides [4], phosphides [5], and nitrides [6,7]. Among them, transition metal oxides have been widely investigated owing to good stability in alkaline media [8]. Especially, Cobalt vanadium oxide showed an interesting property where the V atom shares *d* electrons to promote the metallic behavior [9]. However, this process is restricted by oxides' low instinctive electronic conductivity [10,11]. As a result, increasing the conductivity of metal oxide is necessary for better performance, which can be improved by *N*-doping [12,13]. Because the *N*-doping causes uneven spin density and charge distribution around adjacent atoms, enhancing absorption of reaction intermediates, thereby optimizing OER and HER performance [14,15]. Up to date, fair amounts of studies focusing on *N*-doped Mo- [16], Co– [17], Ni-based [18], sulfides [19–21], oxides [22] and carbides [23,24] were reported. Nevertheless, the HER or OER performance of the reported materials is still inadequate. On the one hand, their performances are far from Pt/C and RuO_2 catalysts [25]. On the other hand, they do not have sufficient stability in the alkaline environment at high current densities (>100 mA cm^{-2}), hindering their industrial application [26]. These limitations could be overcome by the *N*-doping in cobalt vanadium oxide to enhance the conductivity, thereby improving the HER and OER activities.

Here, we reported a series of *N*-doped cobalt vanadium oxides by a facile nitrification process in NH_3. The material exhibited a crystal form of $Co_2V_2O_7$ below 350 °C and would transform into Co_2VO_4/VO_2 at 400 °C or Co_2VO_4/V_2O_3 at 450 °C, respectively. Meanwhile, as the nitrification temperature increased, the nanosheet morphology of the samples gradually became rougher and thicker, affecting the exposure of active sites. Once pyrolysis temperature exceeds 350 °C, the N doping content reaches a maximum value (~2 %). The resulting N-$Co_2V_2O_7$@NF (350 °C) and N-Co_2VO_4/VO_2@NF (400 °C) can be used for OER or HER to achieve overpotentials of 310 mV and 224 mV at 100 mA cm^{-2} to stable for 170 h and 700 h, respectively. Density function theory (DFT) indicates that *N*-doping can distinctly regulate the material's band gap, *d*-band center and absorption/desorption energy of intermediates. Finally, the N-$Co_2V_2O_7$@$NF^{(+)}$||N-Co_2VO_4/VO_2@$NF^{(-)}$ OWS system exhibited a cell voltage of 1.93 V at 500 mA cm^{-2} being superior to RuO_2@$NF^{(+)}$||Pt/C@$NF^{(-)}$ (2.02 V) and can maintain for 60 h with only 1.8 % decline.

2. Experimental section

2.1. Materials

Cobalt chloride hexahydrate ($CoCl_2{\cdot}6H_2O$, 99.5 %, Aladdin, 500 g), ammonium metavanadate (NH_4VO_3, 99.0 %, Aladdin, 100 g), potassium hydroxide (KOH, 90 %, Macklin, 500 g), ethanol (C_2H_5OH, 99.7 %, Xilong, 500 mL), hydrochloric acid (HCl, 37 %, Xilong, 500 mL), commercial Pt/C (20 wt% Pt, Sinero, 1 g), $RuCl_3{\cdot}3H_2O$ (37 %, Inno-chem, 25 g), Nafion solution (5 wt%) and commercial Pt/C (20 wt% Pt, Sinero, 1 g) were purchased from Alfa Aesar. Nickel foam (NF, thickness: 1.6 mm) was obtained from a commercial source. Deionized water was used in the experiments. All chemical reagents were used directly without further purification.

2.2. Synthesis of $Co_2V_2O_7$@NF catalysts

A piece of NF (1.5 × 3.5 cm^2) was washed with 1 M HCl, distilled water and ethanol under ultrasonication for 15 min, respectively, to eliminate surface impurities. Typically, 0.8 mmol $CoCl_2{\cdot}6H_2O$ and 0.8 mmol NH_4VO_3 were dissolved into 30 mL distilled water with persistently stirring at 70 °C for 10 min, respectively. After cooling naturally, above two pieces of solutions were mixed with ultrasonication for 1 h and transferred into a 100 mL autoclave with pretreated NF to heat at 180 °C for 18 h. After cooling, the black NF was taken out, rinsed with distilled water several times and dried overnight (mass loading: 2.0 mg cm^{-2}).

2.3. Synthesis of a serial of N-doping cobalt vanadium oxide catalysts

The as-produced $Co_2V_2O_7$@NF was first loaded into a porcelain boat and inserted into reaction quartz tube to fix in tube furnace. Afterward, the N_2 was introduced for 15 min to exclude the air in this system. Subsequently, NH_3 was flowed into at 300 °C, 350 °C, 400 °C, and 450 °C for 3 h (2 °C min^{-1}), respectively. Waiting until the temperature drops to circumstance temperature, the deep-black produced NF was taken out and named as N-$Co_2V_2O_7$@NF-300, N-$Co_2V_2O_7$@NF, N-Co_2VO_4/VO_2@NF and Co_2VO_4/V_2O_3@NF, respectively (mass loading: 2.1, 2.0, 2.1, and 1.8 mg cm^{-2}, respectively). As a comparison, $Co_2V_2O_7$@NF-350 was synthesized through pyrolysis of $Co_2V_2O_7$@NF at 350 °C for 3 h under an Ar atmosphere.

2.4. Synthesis of RuO_2 and 20 wt% Pt/C electrodes

The $RuCl_3{\cdot}3H_2O$ was directly calcined at 400 °C for 3 h in the air to obtain RuO_2 powders. Then, 2 mg RuO_2 or 20 wt% commercial Pt/C was dispersed into a mixture of 100 μL deionized water, 100 μL ethanol and 5 μL 5 wt% Nafion, respectively. The mixture was ultrasonically treated for at least 30 min to form a uniform catalyst ink, then dropped onto the surface of NF (1 × 1 cm^2) and dried naturally in the air. The corresponding XRD pattern is indexed to RuO_2 (JCPDS: 40–1290), confirming the successful preparation of RuO_2. The SEM image indicates that RuO_2 exists in the form of nanoparticles (Fig. S2).

2.5. Electrochemical tests

Electrochemical tests were conducted in Biologic VMP3 electrochemical workstation with a typical three-electrode system in 1.0 M KOH electrolyte. The catalyst (1 × 1 cm^2), graphite plate and saturated calomel electrode (SCE) were used as working, counter and reference electrode, respectively. Cyclic voltammetry (CV) measurement was performed with a sweep rate of 5 mV s^{-1} at

potentials of − 0.9 to − 1.5 V and 0 to 0.8 V for HER and OER, respectively. Linear sweep voltammetry (LSV) was recorded with a scan rate of 0.2 mV s^{-1} and electrochemical impedance spectroscopy (EIS) test was conducted near the onset potential in the frequency range from 100 kHz to 10 mHz. The electrochemical double layer capacitance (C_{dl}) was obtained by CV tests in a non-faradaic region with scan rates from 2 to 12 mV s^{-1}. Chronopotentiometry measurements achieved the long-term stability test of the catalysts at a current density of 100 mA cm^{-2}. Additionally, the CV was performed with a sweep rate of 5 mV s^{-1} at a potential of 0 to –1.5 V (HER) and 0 to 0.8 V (OER), respectively. All potentials of the reversible hydrogen electrode (RHE) were calibrated by the equation: $E_{RHE} = E_{SCE} + 0.241 + 0.059 \times pH$ (Fig. S1). The OWS test was performed in 1.0 M KOH electrolyte in a potential range of 0 ∼ 2.5 V (vs SCE) with a scan rate of 5 mV s^{-1}.

2.6. Characterization

A scanning electron microscope (SEM, FEI quantum 200 FEG) and transmission electron microscope (TEM, JEM-2100F) characterized the sample's microstructure. X-ray powder diffraction (XRD, D/Max-3c at 12 kW with Cu Kα radiation) patterns were obtained using a scanning speed of 5.0° min^{-1}. The chemical valence states of different elements were certified by X-ray photoelectron spectroscopy (XPS, JPS-9010 Mg Kα). Inductively coupled plasma atomic emission spectrometry (ICP-AES, IRIS Intrepid II XSP) was used to verify the actual loading of different metals in catalysts. The Raman spectrum comes from an in Via confocal Raman microscope (Renishaw, UK). The specific surface area and pore size distribution were calculated according to the Brunauer–Emmett–Teller (BET) and *t*-Plot methods, respectively. The nitrogen content is obtained through an element analyzer (Vario EL III). We performed multiple experiments using elemental analyzers, XPS, and ICP-AES to reduce errors and ensure data accuracy and reproducibility.

3. Result and discussion

N-doped cobalt vanadium oxides sequence was synthesized through a feasible two-step process (Fig. 1a). Initially, $Co_2V_2O_7$ nanosheet precursor was prepared via hydrothermal deposition of $CoCl_2$ and NH_4VO_3 at 180 °C, and the X-ray diffractograms (XRD) is assigned to $Co_2V_2O_7$ (JCPDS: 38–0252). After that, N elements were introduced into $Co_2V_2O_7$ nanosheets along with a phase transformation through pyrolysis at 300 ∼ 450 °C. When the temperature is lower than 350 °C, the $Co_2V_2O_7$ phase persists and converts into Co_2VO_4/VO_2 and Co_2VO_4/V_2O_3 at 400 °C and 450 °C, respectively, which can index well to those of standard cards: $Co_2V_2O_7$ (JCPDS: 38-0252), Co_2VO_4 (JCPDS: 73-1633), VO_2 (JCPDS: 81-2392) and V_2O_3 (JCPDS: 71-0280) (Fig. 1b and S3). Raman spectrum of N-$Co_2V_2O_7$ demonstrates two prominent peaks at 507 and 617 cm^{-1}, corresponding to Co-N and V-N bonds (Fig. 1c) [12,27]. The remaining two located at 266 cm^{-1} and 400 cm^{-1} is identified as V—O and Co—O bonds, respectively [28,29]. Notably, V—O bands of $Co_2V_2O_7$ shift from 277 cm^{-1} to 266 cm^{-1} (N-$Co_2V_2O_7$), indicating that the V-O bond strength change after N doping [30,31]. Brunauer–Emmett–Teller (BET) N_2 adsorption–desorption isotherm displays a typical V-type hysteresis loop, and N-$Co_2V_2O_7$ possesses a mesoporous structure with pore sizes of around 17.9 nm (Fig. S4). In a word, the N element was successfully doped into the $Co_2V_2O_7$ precursor, and the crystal phase of *N*-doped cobalt vanadium oxide strongly depends on the nitrification temperature.

SEM and TEM were used to examine the morphology. After the hydrothermal reaction, $Co_2V_2O_7$ precursor nanosheets densely grow on the NF surface (Fig. 1d). The spacing between nanosheets increased gradually without change of morphology (thick: 5 ∼ 7 nm) at low nitrification temperature (350 °C), which facilitates active site exposure and gas release (Fig. 1e and S5-7a) [32]. Dramatically, the corresponding nanosheet structures became thicker and eventually aggregated together at higher temperatures (400 ∼ 450 °C), indicative of the products' thermal expansion and chemical composition changes (Fig. S7b-c). Note that the $Co_2V_2O_7$@NF-350 material as a control showed almost no noticeable change in morphology after calcination in Ar at 350 °C (Fig. S8). TEM image reveals the well-defined nanosheet structure of N-$Co_2V_2O_7$ and N-Co_2VO_4/VO_2, according to the SEM results (Fig. 1f). In the HRTEM image, interplanar spacings of 0.324 nm, 0.312 nm, and 0.175 nm meet with the (112), (002) and (204) crystal planes of $Co_2V_2O_7$, respectively (Fig. 1g and Fig. S9a). Meanwhile, the HRTEM image of N-Co_2VO_4/VO_2 shows that interplanar spacings of 0.615 nm and 0.296 nm correspond to (001) and (220) crystal planes of VO_2 and Co_2VO_4 (Fig. S9b), respectively. Moreover, the observable interface between the VO_2 and Co_2VO_4 crystal phases indicates the existence of heterostructures. SAED image of N-$Co_2V_2O_7$ reconfirms that the sample possesses a single crystal structure, and the (−111), (−212) and (−112) crystal planes correspond to $Co_2V_2O_7$, respectively (Fig. 1h). HAADF-STEM and corresponding element mapping images reveal that Co, V, O, and N are evenly distributed on the nanosheet (Fig. 1i). Findings mentioned above certify that the N element was triumphantly doped into the sheet-shaped $Co_2V_2O_7$ precursor and can modify the product's morphology under various temperatures.

The chemical states of cobalt vanadium oxides were further explored through XPS. All substances contain obvious Co 2*p*, V 2*p* and O 1 *s* peaks in the full spectrum (Fig. S10). The N content in N-$Co_2V_2O_7$-300 is only 1.0 % from the elemental analyzer, yet in N-$Co_2V_2O_7$-350, N-Co_2VO_4/VO_2-400 and N-Co_2VO_4/V_2O_3-450 are 2.0 %, 2.1 % and 2.1 % without rising apparently, respectively (Table S1). Notably, a small amount of N (about 0.1 %) is present in $Co_2V_2O_7$ due to the NH_4VO_3 precursor, which is insufficient to change the catalytic performance (Table S1 and Fig. S11).

In the Co 2*p* XPS spectra, four peaks are observed at 782.3 eV (Co^{2+} $2p_{3/2}$), 798.1 eV (Co^{2+} $2p_{1/2}$), 780.6 eV (Co^{3+} $2p_{3/2}$) and 796.5 eV (Co^{3+} $2p_{1/2}$) (Fig. 2a), and the content of Co^{2+} is increased slightly with the rising nitrification temperature, which can be ascribed to the reduction properties of NH_3 (Table S2) [33]. V 2*p* spectra display-two doublet peaks at 516.2 eV/523.6 eV and 517.1 eV/524.5 eV, belonging to V^{4+} and V^{5+}, respectively (Fig. 2b) [34,35]. As the nitridation temperature reaches 400 °C, V^{5+} disappears, while V^{3+} appears at the binding energy (515.2 e V/522.6 eV), implying N-$Co_2V_2O_7$ is converted into N-Co_2VO_4 and VO_2 [36]. In the N 1 *s* spectrum, apart from the *N*-metal (*N*-M) bond (397.1 eV) formed by *N*-doping into the oxide, the peak at 399.6 eV originates from the N — H surface terminal group after NH_3 treatment (Fig. 2c) [37–39]. In short, the high-temperature environment can promote N doping into oxide precursors and induce cobalt vanadium oxide's reconstitution.

The catalytic activities of different materials were measured in a 1.0 M KOH solution. As shown in Fig. 3a, three *N*-doped cobalt vanadium catalysts with about 2 % *N*-doping content exhibit catalytic performance comparable to RuO_2. Specifically, N-$Co_2V_2O_7$@NF can achieve the smallest overpotentials of 244 mV, 287 mV and 310 mV to afford current densities of 10, 50, and 100 mA cm^{-2}, respectively, which is visibly better than other catalysts (Fig. S12). Tafel slopes were calculated and displayed in Fig. 3b to understand the reaction mechanism better. The N-$Co_2V_2O_7$@NF presents the smallest Tafel slope of only 56.0 mV dec^{-1} among all catalysts, indicating the fastest OER reaction kinetics [40]. Compared with most recently reported OER electrocata-

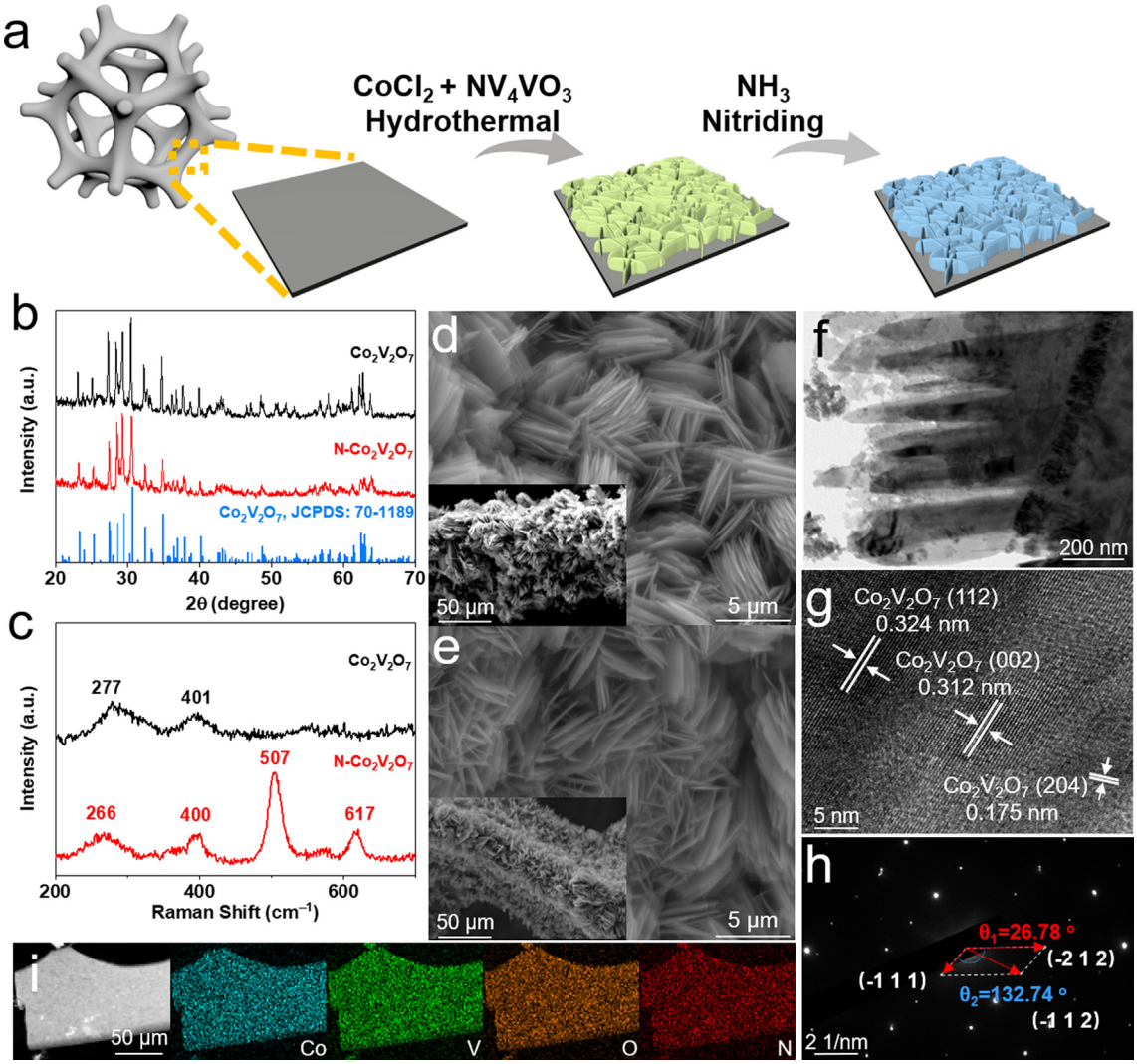

Fig. 1. (a) Schematic illustration of preparing *N*-doped cobalt vanadium oxides on NF. (b) X-ray diffractograms (XRD) and (c) Raman spectra of $Co_2V_2O_7$ and N-$Co_2V_2O_7$. (d-e) Scanning electron microscopy (SEM) images of $Co_2V_2O_7$@NF and N-$Co_2V_2O_7$@NF. (f) Transmission electron microscopy (TEM), (g) high-resolution TEM (HRTEM), (h) selected area electron diffraction (SAED) pattern, and (i) high angle annular dark-field scanning transmission electron microscope (HAADF-TEM) image and corresponding elemental distribution of N-$Co_2V_2O_7$@NF.

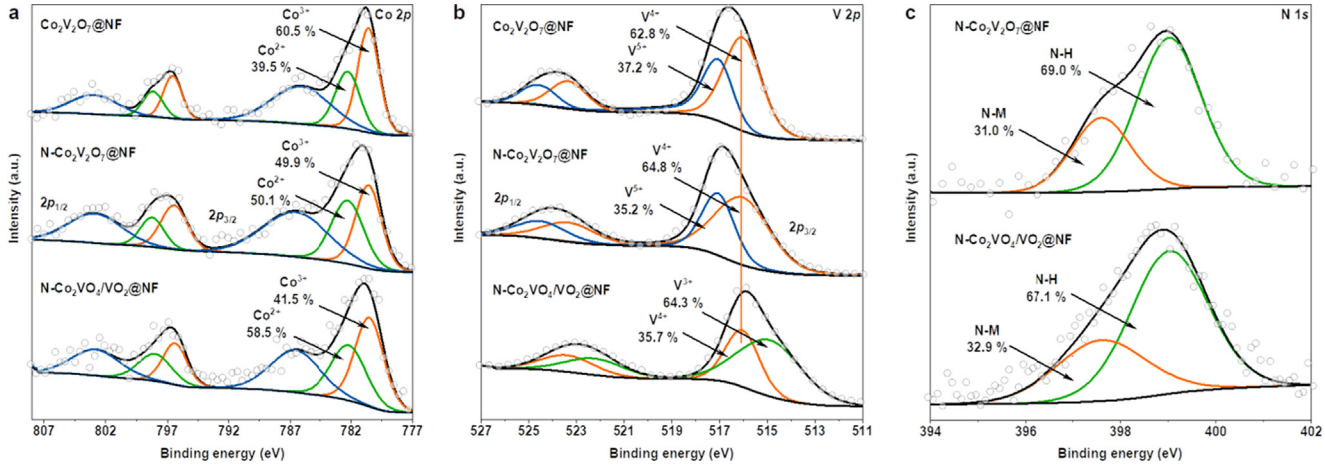

Fig. 2. High-resolution X-ray photoelectron spectra (XPS) of (a) Co 2*p*, (b) V 2*p* and (c) N 1 *s* in $Co_2V_2O_7$@NF, N-$Co_2V_2O_7$@NF and N-Co_2VO_4/VO_2@NF, respectively.

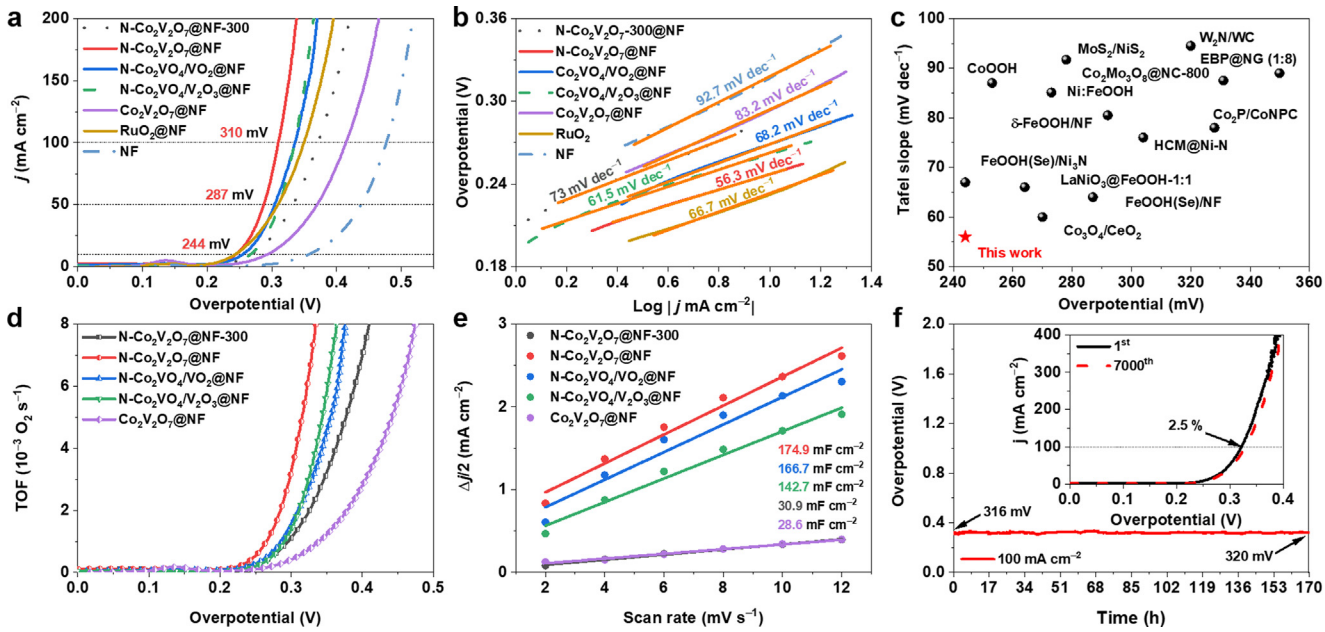

Fig. 3. Electrocatalytic OER performance. (a) OER polarization curves, (b) Tafel plot, and (c) comparison of overpotential at 10 mA cm^{-2} and Tafel of N-$Co_2V_2O_7$@NF with previously reported catalysts. (d) The turnover frequency (TOF) profiles, (e) C_{dl} plots, and (f) chronopotentiometry test in 1.0 M KOH (Inset: polarization curves before and after 7000 CV).

lysts, N-$Co_2V_2O_7$@NF also exhibits superior OER overpotential and Tafel slope (Fig. 3c and Table S3).

TOF values are calculated according to outcomes of inductively coupled plasma atomic emission spectrometry (ICP-AES) (Table S4). Fig. 3d demonstrates the TOF values of the five cobalt-vanadium catalysts at gradually increased applied voltage, and N-$Co_2V_2O_7$@NF possesses the highest TOF value at the same potential, reflecting its robust intrinsic activity [41,42]. Fig. S13 exhibits the TOF values of five cobalt vanadium-based catalysts at 300 mV overpotential. The intrinsic activity of the N-$Co_2V_2O_7$@NF catalyst (N content: 2.0 %) improves about eight times compared with the precursor $Co_2V_2O_7$@NF and three times with N-$Co_2V_2O_7$@NF-300 (N content: 1.0 %), suggesting that *N*-doping plays a crucial role in the intrinsic activity. The electrochemically active surface area (ECSA) and C_{dl} were also calculated (Fig. S14). Similarly, N-$Co_2V_2O_7$@NF displayed the largest ECSA and exposed

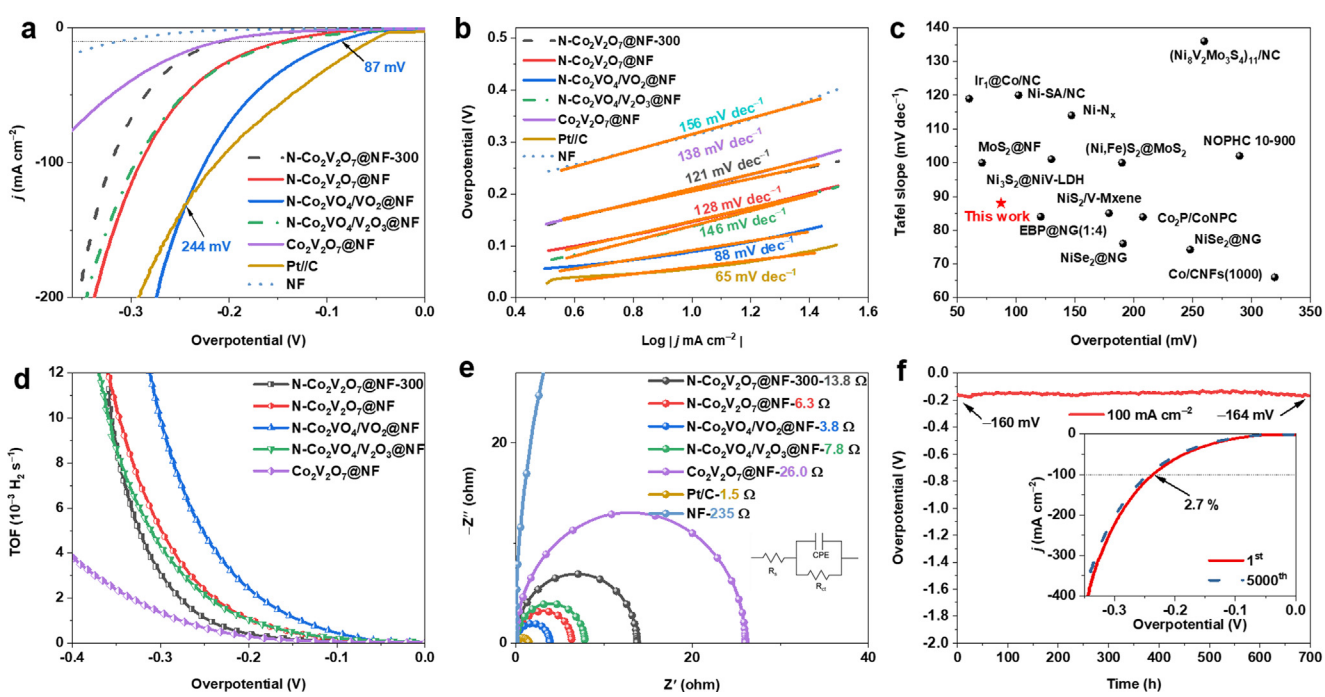

Fig. 4. Electrocatalytic HER performance. (a) HER polarization curves. (b) Tafel slopes. (c) Comparison of overpotential at 10 mA cm^{-2} and Tafel value of N-Co_2VO_4/VO_2@NF with previously reported catalysts. (d) TOF profiles. (e) Nyquist plots (Impedances marked after catalysts are charge transfer resistances). (f) Chronopotentiometry curve (Inset: polarization curves initial and after 5000 CV).

the most active sites, about six times that of $Co_2V_2O_7$@NF and N-$Co_2V_2O_7$@NF-300 (Fig. 3e and S15). Interestingly, neither C_{dl} nor ECSA, $Co_2V_2O_7$@NF-300 (30.9 mF cm^{-2} and 772.5 cm^2) has a slight preponderance over $Co_2V_2O_7$@NF (28.6 mF cm^{-2} and 715 cm^2). To summarize, while the *N*-doping content is low, N will primarily reinforce the intrinsic activity, yet when more N is introduced, it strengthens the inherent activity and increases the number of active.

EIS was used to explore the charge transfer resistance (R_{ct}) relating to the conductivity of the catalyst. The five cobalt vanadium catalysts showed the following sequence: N-$Co_2V_2O_7$@NF (0.7 Ω) < N-Co_2VO_4/V_2O_3@NF (1.3 Ω) < N-Co_2VO_4/VO_2@NF (1.5 Ω) < $Co_2V_2O_7$@NF-300 (2.4 Ω) < $Co_2V_2O_7$@NF (3.1 Ω) (Fig. S16). Obviously, the electrode resistance is visibly reduced after introducing the N element, echoing previous literature [43,44]. In addition, the V can provide d electrons to Co to exhibit stronger catalytic activity [9]. Here, adding the N element can diminish the catalyst's resistance, thereby accelerating this process to ultimately strengthen the intrinsic activity and boost the catalyst's OER performance.

On account of the excellent performance of N-$Co_2V_2O_7$, a long-term stability test at a fixed current density of 100 mA cm^{-2} was executed. The activity only degraded 1.3 % after 170 h (Fig. 3f). Moreover, the stability was also investigated using a multi-cycle CV test (inset: Fig. 3f), appearing that, after 7000 CV cycles, the polarization curve at 100 mA cm^{-2} had decreased by 2.5 %. After the stability test, the nanosheet morphology remained intact (Fig. S17). At the same time, the chemical composition of the catalyst surface changed slightly, in which the proportions of Co^{3+} and V^{5+} increased (from 49.9 % to 67.3 % and 35.2 % to 46.6 %), while *N*-M decreased (from 31 % to 8.2 %). The high-valence states have resulted from the strong oxidation condition of OER (Fig. S18) [20,45].

The HER performance of the catalyst was investigated in a 1.0 M KOH solution. The polarization curves of catalysts have been shown in Fig. 4a. The N-Co_2VO_4/VO_2@NF can achieve an earlier onset potential and a faster current density increase with 87 mV overpotential at 10 mA cm^{-2}, being superior to $Co_2V_2O_7$@NF (208 mV), N-$Co_2V_2O_7$@NF-300 (206 mV), N-$Co_2V_2O_7$@NF (143 mV) and N-Co_2VO_4/V_2O_3@NF (137 mV) (Fig. S19). Notably,

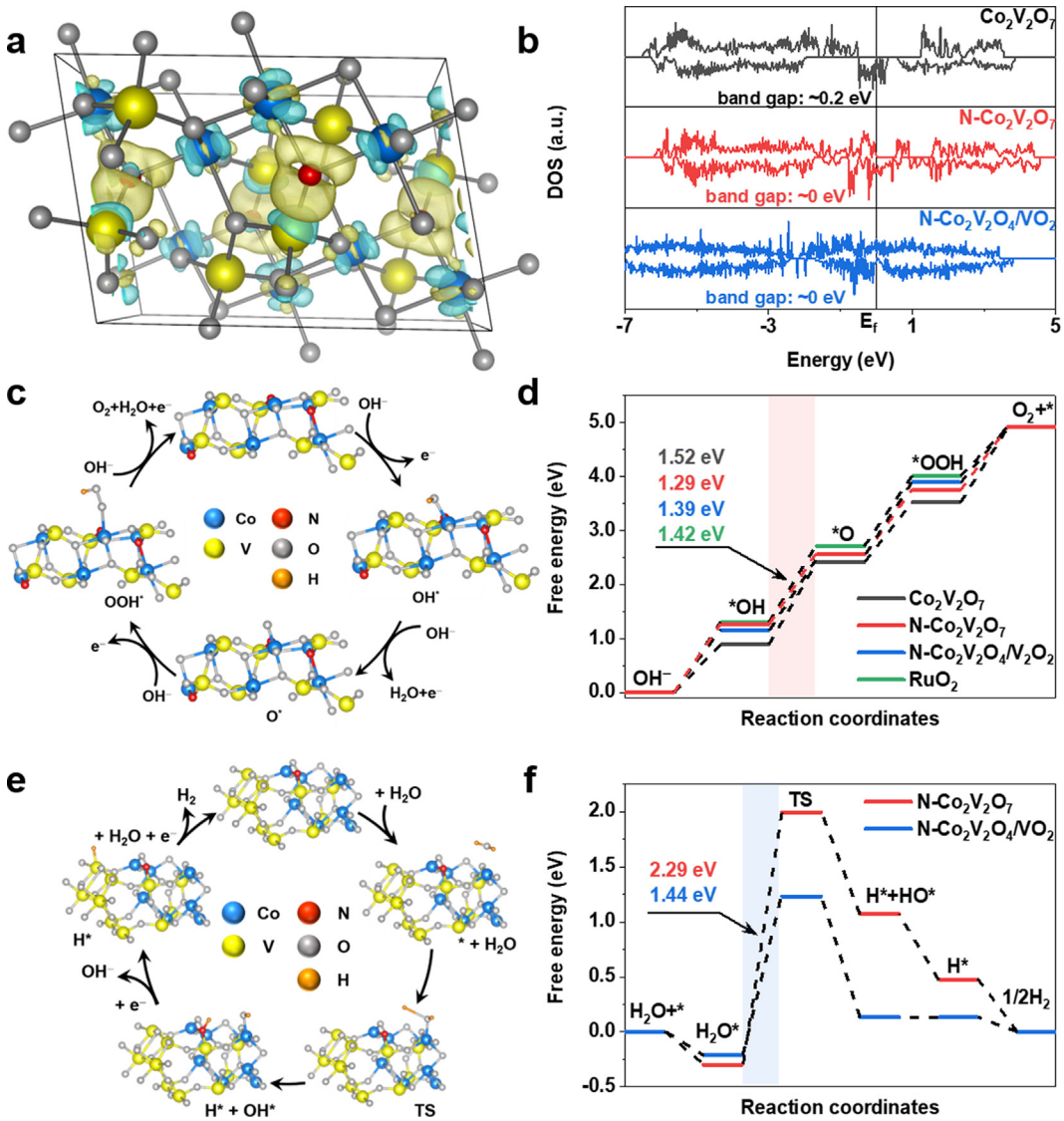

Fig. 5. (a) Differential charge density diagram of N-$Co_2V_2O_7$ (The blue, yellow, red, gray and orange balls represent Co, V, N, O, and H atoms, respectively. Specially, the cyan region represents the depletion of electrons, and the yellow represents the accumulation of electrons.). (b) The density of states (DOS) of different catalysts. (c) OER mechanism illustration of N-$Co_2V_2O_7$. (d) Gibbs free energy diagrams during OER progress. (e) HER mechanism illustration of N-$Co_2V_2O_4$/VO_2. (d) Gibbs free energy diagrams during HER progress.

the N-Co_2VO_4/VO_2@NF outperforms Pt/C@NF when the current density exceeds 130 mA cm^{-2} due to the unique nanosheet structure facilitating electrolyte diffusion and gas emission [46,47]. The Tafel slope corresponding to N-Co_2VO_4/VO_2@NF is 88 mV dec^{-1}, suggesting that its efficient HER kinetics follows the Volmer-Heyrovsky procedure: (1) $M + e^- + H_2O \rightarrow M{-}H^* + OH^-$; (2) $M{-}H^* + e^- + H_2O \rightarrow M + OH^- + H_2$ (Fig. 4b) [48]. Besides, N-Co_2VO_4/VO_2@NF has superior HER activity to most previously reported HER electrocatalysts (Fig. 4c and Table S5).

TOF values also investigated the intrinsic activity of several HER catalysts. As shown in Fig. 4d, with the increase of the applied voltage, the TOF values of five cobalt vanadium-based electrocatalysts rise rapidly. N-Co_2VO_4/VO_2@NF is the most apparent among them, implying that each active site can release the most significant number of H_2 molecules per second [5]. The EIS shown in Fig. 4e demonstrates that the R_{ct} of N-Co_2VO_4/VO_2@NF is 3.8 Ω, second only to Pt/C@NF (1.5 Ω), implying high conductivity during the HER process.

Ultimately, long-term testing of N-Co_2VO_4/VO_2@NF was conducted and can stabilize for 700 h at a current density of 100 mA cm^{-2} with minor deterioration (Fig. 4f). Furthermore, after 5000 CV cycle tests, the overpotential increased by only 2.7 % at 100 mA cm^{-2} (inset: Fig. 4f). Notably, the morphology and chemical states of the catalyst did not change evidently after the stability test, conforming the superior stability of catalyst (Fig. S20-S21).

DFT calculations were performed to understand further the enhanced function of N doping toward electrocatalyst activity. After N doping, substantial charge redistribution occurs in N-$Co_2V_2O_7$ and N-$Co_2V_2O_4/VO_2$, and most of the charges accumulate around N, which favors the subsequent electron transfer and absorption/desorption intermediates (Fig. 5a and S22) [49]. To sight more about the origin of the high intrinsic activity after introducing the N element, DOS was employed. N-$Co_2V_2O_7$ and N-$Co_2V_2O_4/VO_2$ confirm significantly contracted band gaps, corresponding to reinforced electrical conductivity after *N*-doping (Fig. 5b) [50–52]. Meanwhile, N-$Co_2V_2O_7$ possesses a more positive d-band center (−0.74 eV) than $Co_2V_2O_7$ (−1.11 eV), suggesting more favorable adsorption of active intermediate [53]. The OER mechanism and corresponding Gibbs free energy diagram are illustrated in Fig. 5c and 5d. First, OH^- loses an electron by attaching to the Co site; next, a proton is attacked by another OH^-, and then deprotonates to form *OOH [54]. Finally, the proton-coupled electron transfer leads to the release of O_2 [55]. In these, the rate-determining step (RDS) is the second step ($*OH + OH^- \rightarrow *O + H_2O + e^-$). The N-$Co_2V_2O_7$ shows the smallest reaction Gibbs free energy (1.29 eV) compared with 1.52 eV on $Co_2V_2O_7$, indicating that the electronic structure and d-band center of the catalyst can be controlled by doping N element into $Co_2V_2O_7$, resulting in a calculated free energy closer to the optimal value of 1.23 eV, thus devoting to improved OER performance (Table S6) [56].

Fig. 5e and 5f depict the HER mechanism and corresponding Gibbs free energy diagram, where N-$Co_2V_2O_4/VO_2$ display a clear shrinkage trend implying a more favorable HER pathway [57]. Typically, the activation of the H_2O toward the transition state (TS) serves as the RDS for HER, and N-$Co_2V_2O_4/VO_2$ exhibits a more desirable energy barrier of 1.44 eV than N-$Co_2V_2O_7$ (2.29 eV), inferring a synergistic effect at N-$Co_2V_2O_4/VO_2$ interface can significantly accelerate the absorption of H_2O (Table S7) [58]. Additionally, as diverse adsorption capacities of various sites for different intermediates, a hydrogen spillover phenomenon occurs on N-$Co_2V_2O_4/VO_2$ during the Heyrovsky step, which can regulate the activated site of H^* to moderate hydrogen binding energy, 0.13 eV for N-$Co_2V_2O_4/VO_2$, which closes to the ideal value (0 eV) [59–61]. This noticeable difference can be attributed to the synergistic effects in N-$Co_2V_2O_4/VO_2$ interface and the hydrogen spillover phenomenon caused by *N*-doping, which can gear up H_2O-activation and balance the H^* adsorption and subsequent H_2 desorption, respectively, resulting in better HER performance.

Considering the extraordinary OER and HER activity of *N*-doped cobalt vanadium oxides, an OWS system was assembled by using N-$Co_2V_2O_7$@NF as anode and N-$Co_2V_2O_4/VO_2$@NF as the cathode (Fig. 6a). This device only needs a cell voltage of 1.52 V at 10 mA cm^{-2} being equivalent to the RuO_2@$NF^{(+)}$||Pt/C@$NF^{(-)}$ (1.51 V) (Fig. 6b-c). Simultaneously, this N-$Co_2V_2O_7$@$NF^{(+)}$||N-

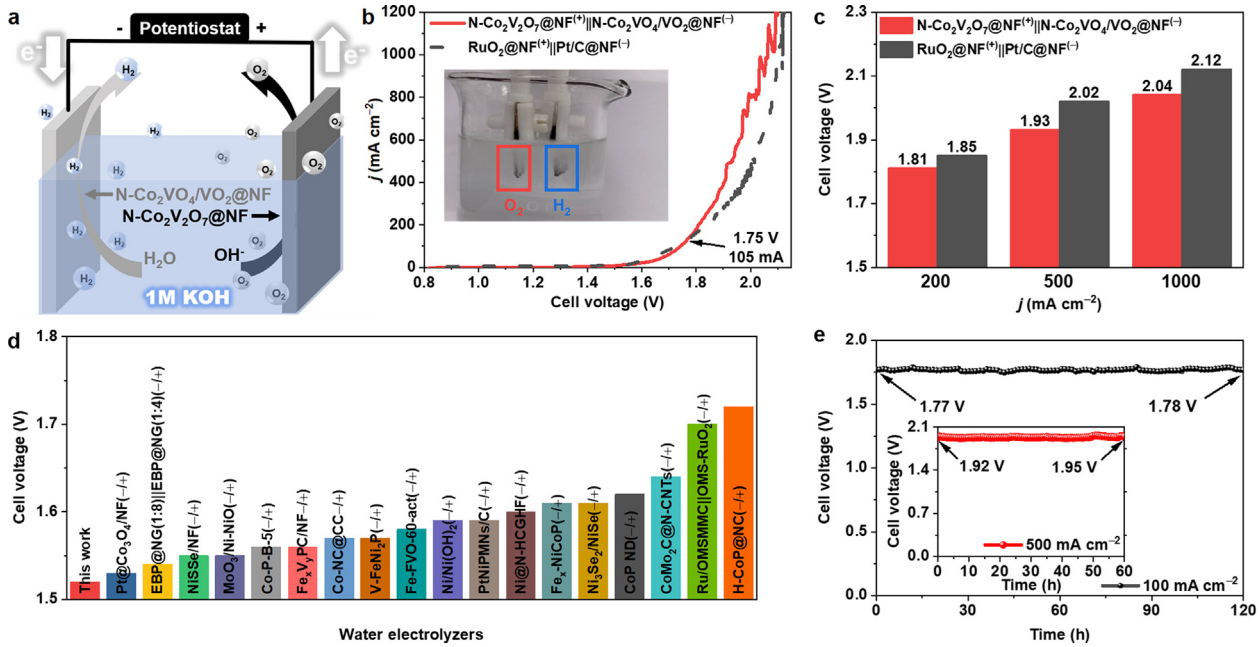

Fig. 6. (a) Schematic diagram of OWS system. (b) Polarization curves of N-$Co_2V_2O_7$@$NF^{(+)}$||N-Co_2VO_4/VO_2@$NF^{(-)}$ and RuO_2@$NF^{(+)}$||Pt/C@$NF^{(-)}$ in 1.0 M KOH electrolyte. (c) Comparison of cell voltages for OWS system at 200, 300, and 1000 mA cm^{-2}. (d) Comparison of the alkaline OWS activity with previous reports at 10 mA cm^{-2}. (e) Chronopotentiometry tests at 100 and 500 mA cm^{-2}.

$Co_2V_2O_4/VO_2$@NF$^{(-)}$ OWS system was compared to the newly reported cell voltage of the two-electrode devices at 10 mA cm^{-2}, suggesting that it outperforms most systems (Fig. 6d). In addition, once the applied voltage exceeds 1.75 V, N-$Co_2V_2O_7$@NF$^{(+)}$||N- Co_2-V_2O_4/VO_2@NF$^{(-)}$ requires less voltage to achieve the same current density than RuO_2@NF $^{(+)}$||Pt/C@NF$^{(-)}$. Moreover, this water electrolysis device can be stabilized for 120 h at 100 mA cm^{-2} with a voltage loss of 0.11 % and only changed 1.8 % after 60 h at 500 mA cm^{-2} (Fig. 6e-f).

Based on the above discussions, this excellent OER activity of the N-$Co_2V_2O_7$@NF catalyst can be ascribed to the following factors: (1) Vertical nanosheet arrangement can speed up electrolyte transport and gas emissions. (2) The combination of cobalt and vanadium bimetal can enhance the activity of metal sites. (3) *N*-doping can promote charge transfer and regulate the adsorption of intermediates. For HER, *N* doping is only part of the reason for improving performance, and the formation of the N-$Co_2V_2O_4/VO_2$ interface is also a non-negligible reason.

4. Conclusion

In summary, we fabricated cobalt vanadium oxide nanosheet series by hydrothermal and nitrification processes. The results revealed that the nitrification temperature significantly influenced the catalysts' microstructure and crystallinity. The maximum *N*-doping (about 2 %) was achieved after nitrification temperature exceeded 350 °C. Electrochemical tests found that N-$Co_2V_2O_7$@NF prepared at 350 °C and N-Co_2VO_4/VO_2@NF prepared at 400 °C had the best OER and HER electrocatalytic activities and stabilities among all catalysts, respectively. Impressively, overall water splitting assembled by N-$Co_2V_2O_7$@NF$^{(+)}$||N-Co_2VO_4/VO_2@NF$^{(-)}$ can achieve a cell voltage of 1.93 V@500 mA cm^{-2} even superior to RuO_2@NF$^{(+)}$||Pt/C@NF$^{(-)}$ (2.02 V). The DFT study indicates that *N*-doping can reduce the band gap of materials and promote the adsorption/desorption of intermediates, resulting in faster charge transfer and smaller reaction energy barriers. Notably, hydrogen spillover occurs at the N-Co_2VO_4/VO_2 interface, leading to a more desirable binding energy for H_{ad}, making the HER performance more ideal. This work provides a feasible strategy for constructing highly efficient *N*-doped electrocatalysts for industrial applications.

CRediT authorship contribution statement

Zuyang Luo: Conceptualization, Writing – original draft. **Qimin Peng:** Data curation. **Zhiyang Huang:** Visualization. **Lixia Wang:** Investigation. **Yuting Yang:** Software. **Jiaxin Dong:** Data curation. **Tayirjan Taylor Isimjan:** Writing – review & editing. **Xiulin Yang:** Supervision, Writing – review & editing.

Data availability

Data will be made available on request.

Declaration of Competing Interest

The authors declare that they have no known competing financial interests or personal relationships that could have appeared to influence the work reported in this paper.

Acknowledgements

This work has been supported by the National Natural Science Foundation of China (no. 21965005), Natural Science Foundation of Guangxi Province (2018GXNSFAA294077, 2020JJYGA120084), Guangxi Science and Technology Plan Project (Guike AD20297039), Project of High-Level Talents of Guangxi (F-KA18015, 2018ZD004), and Guangxi Technology Base and Talent Subject (GUIKE AD18126001).

Data availability

The data that support the findings of this study are available from the corresponding author upon request.

Appendix A. Supplementary material

Supplementary data to this article can be found online at https://doi.org/10.1016/j.jcis.2022.09.069.

References

[1] B. Zhang, Y. Zheng, T. Ma, C. Yang, Y. Peng, Z. Zhou, M. Zhou, S. Li, Y. Wang, C. Cheng, Designing MOF Nanoarchitectures for Electrochemical Water Splitting, Adv. Mater. 33 (2021) 2006042, https://doi.org/10.1002/adma.202006042.
[2] T.X. Nguyen, Y.C. Liao, C.C. Lin, Y.H. Su, J.M. Ting, Advanced High Entropy Perovskite Oxide Electrocatalyst for Oxygen Evolution Reaction, Adv. Funct. Mater. 31 (2021) 2101632, https://doi.org/10.1002/adfm.202101632.
[3] M. Saruyama, C.M. Pelicano, T. Teranishi, Bridging electrocatalyst and cocatalyst studies for solar hydrogen production via water splitting, Chem. Sci. 13 (2022) 2824, https://doi.org/10.1039/d1sc06015e.
[4] X. Li, Y. Wang, J. Wang, Y. Da, J. Zhang, L. Li, C. Zhong, Y. Deng, X. Han, W. Hu, Sequential Electrodeposition of Bifunctional Catalytically Active Structures in MoO_3/Ni-NiO Composite Electrocatalysts for Selective Hydrogen and Oxygen Evolution, Adv. Mater. 32 (2020) 2003414, https://doi.org/10.1002/adma.202003414.
[5] H. Yu, L. Qi, Y. Hu, Y. Qu, P. Yan, T.T. Isimjan, X. Yang, Nanowire-structured FeP-CoP arrays as highly active and stable bifunctional electrocatalyst synergistically promoting high-current overall water splitting, J. Colloid Interface Sci. 600 (2021) 811, https://doi.org/10.1016/j.jcis.2021.05.074.
[6] Y. Zhong, Y. Lu, Z. Pan, J. Yang, G. Du, J. Chen, Q. Zhang, H. Zhou, J. Wang, C. Wang, W. Li, Efficient Water Splitting System Enabled by Multifunctional Platinum-Free Electrocatalysts, Adv. Funct. Mater. 31 (2021) 2009853, https://doi.org/10.1002/adfm.202009853.
[7] Y. Hu, M. Guo, C. Hu, J. Dong, P. Yan, T. Taylor Isimjan, X. Yang, Engineering cobalt nitride nanosheet arrays with rich nitrogen defects as a bifunctional robust oxygen electrocatalyst in rechargeable Zn-air batteries, J. Colloid Interface Sci. 608 (2022) 2066, https://doi.org/10.1016/j.jcis.2021.10.128.
[8] Y. Yang, R. Zeng, Y. Xiong, F.J. DiSalvo, H.D. Abruna, Cobalt-Based Nitride-Core Oxide-Shell Oxygen Reduction Electrocatalysts, J. Am. Chem. Soc. 141 (2019) 19241, https://doi.org/10.1021/jacs.9b10809.
[9] C. Mu, J. Mao, J. Guo, Q. Guo, Z. Li, W. Qin, Z. Hu, K. Davey, T. Ling, S.Z. Qiao, Rational Design of Spinel Cobalt Vanadate Oxide Co_2VO_4 for Superior Electrocatalysis, Adv. Mater. 32 (2020) 1907168, https://doi.org/10.1002/adma.201907168.
[10] Y. Yang, H. Peng, Y. Xiong, Q. Li, J. Lu, L. Xiao, F.J. DiSalvo, L. Zhuang, H.D. Abruña, High-Loading Composition-Tolerant Co–Mn Spinel Oxides with Performance beyond 1 W/cm^2 in Alkaline Polymer Electrolyte Fuel Cells, ACS Energy Lett. 4 (2019) 1251, https://doi.org/10.1021/acsenergylett.9b00597.
[11] R. Yu, H. Zhang, B. Guo, Conductive Biomaterials as Bioactive Wound Dressing for Wound Healing and Skin Tissue Engineering, Nanomicro Lett. 14 (2021) 1, https://doi.org/10.1007/s40820-021-00751-y.
[12] D. Guo, Z. Zeng, Z. Wan, Y. Li, B. Xi, C. Wang, A CoN-based OER Electrocatalyst Capable in Neutral Medium: Atomic Layer Deposition as Rational Strategy for Fabrication, Adv. Funct. Mater. 31 (2021) 2101324, https://doi.org/10.1002/adfm.202101324.
[13] C.-L. Zhang, Y. Xie, J.-T. Liu, F.-H. Cao, H.-P. Cong, H. Li, 1D Core−Shell MOFs derived CoP Nanoparticles-Embedded N-doped porous carbon nanotubes anchored with MoS_2 nanosheets as efficient bifunctional electrocatalysts, Chem. Eng. J. 419 (2021), https://doi.org/10.1016/j.cej.2021.129977 129977.
[14] C. Pi, C. Huang, Y. Yang, H. Song, X. Zhang, Y. Zheng, B. Gao, J. Fu, P.K. Chu, K. Huo, In situ formation of N-doped carbon-coated porous MoP nanowires: a highly efficient electrocatalyst for hydrogen evolution reaction in a wide pH range, Appl. Catal. B: Environ. 263 (2020) 118358, doi: 10.1016/j.apcatb.2019.118358.
[15] X.-Z. Fan, Q.-Q. Pang, S.-S. Yi, X. Du, S. Zhang, Z.-Y. Liu, X.-Z. Yue, Intrinsic-structural-modulated carbon cloth as efficient electrocatalyst for water oxidation, Appl. Catal. B: Environ. 292 (2021) 120152, doi: 10.1016/j.apcatb.2021.120152.
[16] Y.Y. Chen, Y. Zhang, W.J. Jiang, X. Zhang, Z. Dai, L.J. Wan, J.S. Hu, Pomegranate-like N, P-Doped Mo_2C@C Nanospheres as Highly Active Electrocatalysts for Alkaline Hydrogen Evolution, ACS Nano 10 (2016) 8851, https://doi.org/10.1021/acsnano.6b04725.
[17] P. Yan, Y. Hu, E. Shoko, T.T. Isimjan, J. Tian, X. Yang, Hierarchical Core-Shell N-Doped Carbon@FeP_4-CoP Arrays as Robust Bifunctional Electrocatalysts for

Overall Water Splitting at High Current Density, Adv. Mater. Interfaces 8 (2021) 2100065, https://doi.org/10.1002/admi.202100065.
[18] P. Balasubramanian, S.-B. He, A. Jansirani, H.-H. Deng, H.-P. Peng, X.-H. Xia, W. Chen, Engineering of oxygen vacancies regulated core-shell N-doped carbon@$NiFe_2O_4$ nanospheres: A superior bifunctional electrocatalyst for boosting the kinetics of oxygen and hydrogen evaluation reactions, Chem. Eng. J. 405 (2021), https://doi.org/10.1016/j.cej.2020.126732 126732.
[19] C. Deng, K.-H. Wu, J. Scott, S. Zhu, R. Amal, D.-W. Wang, Ternary MnO/CoMn alloy@N-doped graphitic composites derived from a bi-metallic pigment as bi-functional electrocatalysts, J. Mater. Chem. A 7 (2019) 20649, https://doi.org/10.1039/c9ta08016c.
[20] Q. Peng, X. Shao, C. Hu, Z. Luo, T. Taylor Isimjan, Z. Dou, R. Hou, X. Yang, Co_4S_3 grafted 1 T-phase dominated WS_2 ultrathin nanosheet arrays for highly efficient overall water splitting in alkaline media, J. Colloid Interface Sci. 615 (2022) 577, doi: 10.1016/j.jcis.2022.02.031.
[21] W.-H. Huang, X.-M. Li, X.-F. Yang, H.-Y. Zhang, P.-B. Liu, Y.-M. Ma, X. Lu, CeO2-embedded mesoporous CoS/MoS_2 as highly efficient and robust oxygen evolution electrocatalyst, Chem. Eng. J. 420 (2021), https://doi.org/10.1016/j.cej.2020.127595 127595.
[22] K. Dai, N. Zhang, L. Zhang, L. Yin, Y. Zhao, B. Zhang, Self-supported Co/CoO anchored on N-doped carbon composite as bifunctional electrocatalyst for efficient overall water splitting, Chem. Eng. J. 414 (2021), https://doi.org/10.1016/j.cej.2021.128804 128804.
[23] H. Zhang, Y. Liu, T. Chen, J. Zhang, J. Zhang, X.W.D. Lou, Unveiling the Activity Origin of Electrocatalytic Oxygen Evolution over Isolated Ni Atoms Supported on a N-Doped Carbon Matrix, Adv. Mater. 31 (2019) 1904548, https://doi.org/10.1002/adma.201904548.
[24] W. Huang, W. Gao, S. Zuo, L. Zhang, K. Pei, P. Liu, R. Che, H. Zhang, Hollow MoC/NC sphere for electromagnetic wave attenuation: direct observation of interfacial polarization on nanoscale hetero-interfaces, J. Mater. Chem. A. 10 (2022) 1290, https://doi.org/10.1039/d1ta09357f.
[25] X. Li, J. Zhou, C. Liu, L. Xu, C. Lu, J. Yang, H. Pang, W. Hou, Encapsulation of Janus-structured Ni/Ni_2P nanoparticles within hierarchical wrinkled N-doped carbon nanofibers: Interface engineering induces high-efficiency water oxidation, Appl. Catal. B: Environm. 298 (2021), https://doi.org/10.1016/j.apcatb.2021.120578 120578.
[26] F. Guo, Z. Zou, Z. Zhang, T. Zeng, Y. Tan, R. Chen, W. Wu, N. Cheng, X. Sun, Confined sub-nanometer PtCo clusters as a highly efficient and robust electrocatalyst for the hydrogen evolution reaction, J. Mater. Chem. A 9 (2021) 5468, https://doi.org/10.1039/d0ta10500g.
[27] X. Zhao, Q. Han, J. Li, X. Du, G. Liu, Y. Wang, L. Wu, Z. Chen, Ordered macroporous design of sacrificial Co/VN nano-heterojunction as bifunctional oxygen electrocatalyst for rechargeable zinc-air batteries, Chem. Eng. J. 433 (2021), https://doi.org/10.1016/j.cej.2021.133509 133509.
[28] X. He, C. Zhang, D. Tian, The Structure, Vibrational Spectra, and Thermal Expansion Study of AVO_4 (A=Bi, Fe, Cr) and $Co_2V_2O_7$, Materials 13 (2020) 1628, https://doi.org/10.3390/ma13071628.
[29] C. Jiang, J. Yang, T. Zhao, L. Xiong, Z.-X. Guo, Y. Ren, H. Qi, A. Wang, J. Tang, Co^{3+}-O-V^{4+} cluster in $CoVO_x$ nanorods for efficient and stable electrochemical oxygen evolution, Appl. Catal. B: Environ. 282 (2021), https://doi.org/10.1016/j.apcatb.2020.119571 119571.
[30] Y.H. Wang, S. Zheng, W.M. Yang, R.Y. Zhou, Q.F. He, P. Radjenovic, J.C. Dong, S. Li, J. Zheng, Z.L. Yang, G. Attard, F. Pan, Z.Q. Tian, J.F. Li, In situ Raman spectroscopy reveals the structure and dissociation of interfacial water, Nature 600 (2021) 81, https://doi.org/10.1038/s41586-021-04068-z.
[31] Y. Dai, J. Yu, J. Wang, Z. Shao, D. Guan, Y.C. Huang, M. Ni, Bridging the Charge Accumulation and High Reaction Order for High-Rate Oxygen Evolution and Long Stable Zn-Air Batteries, Adv. Funct. Mater. 32 (2022) 2111989, https://doi.org/10.1002/adfm.202111989.
[32] X. Jin, T.-H. Gu, K.-G. Lee, M.J. Kim, M.S. Islam, S.-J. Hwang, Unique advantages of 2D inorganic nanosheets in exploring high-performance electrocatalysts: Synthesis, application, and perspective, Coord. Chem. Rev. 415 (2020), https://doi.org/10.1016/j.ccr.2020.213280 213280.
[33] W. Huang, J. Chen, W. Gao, L. Wang, P. Liu, Y. Zhang, Z. Yin, Y. Yang, "Host-Guest" crystalline Mo/Co-framework induced phase-conversion of MoCx in carbon hybrids for regulating absorption of electromagnetic wave, Carbon 197 (2022) 129–140, https://doi.org/10.1016/j.carbon.2022.06.031.
[34] N. Suo, Z. Dou, L. Cui, Interface and composition engineering of vanadium doped cobalt nickel sulfide/phosphide heterostructure for efficient water splitting, Electrochim. Acta 368 (2021), https://doi.org/10.1016/j.electacta.2020.137602 137602.
[35] M. Sakthivel, S. Ramaraj, S.-M. Chen, K.-C. Ho, Bimetallic vanadium cobalt diselenide nanosheets with additional active sites for excellent asymmetric pseudocapacitive performance: comparing the electrochemical performances with M-$CoSe_2$ (M = Zn, Mn, and Cu), J. Mater. Chem. A 7 (2019) 12565, https://doi.org/10.1039/c9ta03024g.
[36] P. Zhou, X. Lv, D. Xing, F. Ma, Y. Liu, Z. Wang, P. Wang, Z. Zheng, Y. Dai, B. Huang, High-efficient electrocatalytic overall water splitting over vanadium doped hexagonal $Ni_{0.2}Mo_{0.8}N$, Appl. Catal. B: Environ. 263 (2020) 118330, doi: 10.1016/j.apcatb.2019.118330.
[37] Z. Liu, D. Liu, L. Zhao, J. Tian, J. Yang, L. Feng, Efficient overall water splitting catalyzed by robust $FeNi_3N$ nanoparticles with hollow interiors, J. Mater. Chem. A 9 (2021) 7750, https://doi.org/10.1039/d1ta01014j.
[38] X. Shao, Y. Yang, Y. Liu, P. Yan, S. Zhou, T. Taylor Isimjan, X. Yang, Oxygen vacancy-rich N-doped carbon encapsulated BiOCl-CNTs heterostructures as robust electrocatalyst synergistically promote oxygen reduction and Zn-air batteries, J. Colloid Interface Sci. 607 (2022) 826, doi: 10.1016/j.jcis.2021.08.210.
[39] W. Huang, S. Wang, X. Yang, X. Zhang, Y. Zhang, K. Pei, R. Che, Temperature induced transformation of Co@C nanoparticle in 3D hierarchical core-shell nanofiber network for enhanced electromagnetic wave adsorption, Carbon 195 (2022) 44–56, https://doi.org/10.1016/j.carbon.2022.04.019.
[40] B. Li, Z. Li, Q. Pang, J.Z. Zhang, Core/shell cable-like Ni_3S_2 nanowires/N-doped graphene-like carbon layers as composite electrocatalyst for overall electrocatalytic water splitting, Chem. Eng. J. 401 (2020), https://doi.org/10.1016/j.cej.2020.126045 126045.
[41] L. Yang, H. Liu, H. Shen, Y. Huang, S. Wang, L. Zheng, D. Cao, Physically Adsorbed Metal Ions in Porous Supports as Electrocatalysts for Oxygen Evolution Reaction, Adv. Funct. Mater. 30 (2020) 1909889, https://doi.org/10.1002/adfm.201909889.
[42] M.Y. Ye, S. Li, X. Zhao, N.V. Tarakina, C. Teutloff, W.Y. Chow, R. Bittl, A. Thomas, Cobalt-Exchanged Poly(Heptazine Imides) as Transition Metal-Nx Electrocatalysts for the Oxygen Evolution Reaction, Adv. Mater. 32 (2020) 1903942, https://doi.org/10.1002/adma.201903942.
[43] Y. Cheng, H. Guo, P. Yuan, X. Li, L. Zheng, R. Song, Self-supported bifunctional electrocatalysts with Ni nanoparticles encapsulated in vertical N-doped carbon nanotube for efficient overall water splitting, Chem. Eng. J. 411 (2021), https://doi.org/10.1016/j.cej.2020.127531 127531.
[44] J. Wang, R. Zhu, J. Cheng, Y. Song, M. Mao, F. Chen, Y. Cheng, Co, Mo_2C encapsulated in N-doped carbon nanofiber as self-supported electrocatalyst for hydrogen evolution reaction, Chem. Eng. J. 397 (2020), https://doi.org/10.1016/j.cej.2020.125481 125481.
[45] H. Ma, Z. Chen, Z. Wang, C.V. Singh, Q. Jiang, Interface Engineering of Co/CoMoN/NF Heterostructures for High-Performance Electrochemical Overall Water Splitting, Adv. Sci. 9 (2022) 2105313, https://doi.org/10.1002/advs.202105313.
[46] M. Guo, A. Qayum, S. Dong, X. Jiao, D. Chen, T. Wang, In situ conversion of metal (Ni, Co or Fe) foams into metal sulfide (Ni_3S_2, Co_9S_8 or FeS) foams with surface grown N-doped carbon nanotube arrays as efficient superaerophobic electrocatalysts for overall water splitting, J. Mater. Chem. A 8 (2020) 9239, https://doi.org/10.1039/D0TA02337J.
[47] Z. Abdin, C.J. Webb, E.M. Gray, Modelling and simulation of an alkaline electrolyser cell, Energy 138 (2016) 316, https://doi.org/10.1016/j.energy.2017.07.053.
[48] K. Kim, A.P. Tiwari, G. Hyun, Y. Yoon, H. Kim, J.Y. Park, K.-S. An, S. Jeon, Continuous 3D-nanopatterned Ni–Mo solid solution as a free-standing electrocatalyst for the hydrogen evolution reaction in alkaline medium, J. Mater. Chem. A 9 (2021) 7767, https://doi.org/10.1039/d0ta12466d.
[49] Y. Niu, X. Teng, S. Gong, Z. Chen, A bimetallic alloy anchored on biomass-derived porous N-doped carbon fibers as a self-supporting bifunctional oxygen electrocatalyst for flexible Zn–air batteries, J. Mater. Chem. A 8 (2020) 13725, https://doi.org/10.1039/d0ta03288c.
[50] T.L.L. Doan, D.C. Nguyen, S. Prabhakaran, D.H. Kim, D.T. Tran, N.H. Kim, J.H. Lee, Single-Atom Co-Decorated MoS_2 Nanosheets Assembled on Metal Nitride Nanorod Arrays as an Efficient Bifunctional Electrocatalyst for pH-Universal Water Splitting, Adv. Funct. Mater. 31 (2021) 2100233, https://doi.org/10.1002/adfm.202100233.
[51] L. An, Y. Hu, J. Li, J. Zhu, M. Sun, B. Huang, P. Xi, C.H. Yan, Tailoring Oxygen Reduction Reaction Pathway on Spinel Oxides via Surficial Geometrical-Site Occupation Modification Driven by the Oxygen Evolution Reaction, Adv. Mater. 34 (2022) 2202874, https://doi.org/10.1002/adma.202202874.
[52] M. Lu, Y. Zheng, Y. Hu, B. Huang, D. Ji, M. Sun, J. Li, Y. Peng, R. Si, P. Xi, C.-H. Yan, Artificially steering electrocatalytic oxygen evolution reaction mechanism by regulating oxygen defect contents in perovskites, Sci. Adv. 8 (2022) eabq3563, https://doi.org/10.1126/sciadv.abq3563.
[53] C. Zhou, X. Chen, S. Liu, Y. Han, H. Meng, Q. Jiang, S. Zhao, F. Wei, J. Sun, T. Tan, R. Zhang, Superdurable Bifunctional Oxygen Electrocatalyst for High-Performance Zinc-Air Batteries, J. Am. Chem. Soc. 144 (2022) 2694, https://doi.org/10.1021/jacs.1c11675.
[54] Y. Wang, X. Li, M. Zhang, J. Zhang, Z. Chen, X. Zheng, Z. Tian, N. Zhao, X. Han, K. Zaghib, Y. Wang, Y. Deng, W. Hu, Highly Active and Durable Single-Atom Tungsten-Doped $NiS_{0.5}Se_{0.5}$ Nanosheet@$NiS_{0.5}Se_{0.5}$ Nanorod Heterostructures for Water Splitting, Adv. Mater. 34 (2022) 2107053, https://doi.org/10.1002/adma.202107053.
[55] L. Zhang, W. Cai, N. Bao, Top-Level Design Strategy to Construct an Advanced High-Entropy Co-Cu-Fe-Mo (Oxy)Hydroxide Electrocatalyst for the Oxygen Evolution Reaction, Adv. Mater. 33 (2021) 2100745, https://doi.org/10.1002/adma.202100745.
[56] S. Li, Y. Gao, N. Li, L. Ge, X. Bu, P. Feng, Transition metal-based bimetallic MOFs and MOF-derived catalysts for electrochemical oxygen evolution reaction, Energy Environ. Sci 14 (2021) 1897, https://doi.org/10.1039/d0ee03697h.
[57] L. Zhai, X. She, L. Zhuang, Y. Li, R. Ding, X. Guo, Y. Zhang, Y. Zhu, K. Xu, H.J. Fan, S.P. Lau, Modulating Built-In Electric Field via Variable Oxygen Affinity for Robust Hydrogen Evolution Reaction in Neutral Media, Angew. Chem. Int. Ed. 61 (2022) 202116057, https://doi.org/10.1002/anie.202116057.
[58] W. Wu, Z. Zhang, Z. Lei, X. Wang, Y. Tan, N. Cheng, X. Sun, Encapsulating Pt Nanoparticles inside a Derived Two-Dimensional Metal-Organic Frameworks for the Enhancement of Catalytic Activity, ACS Appl. Mater. Interfaces 12 (2020) 10359, https://doi.org/10.1021/acsami.9b20781.
[59] G. Kyriakou, M.B. Boucher, A.D. Jewell, E.A. Lewis, T.J. Lawton, A.E. Baber, H.L. Tierney, M. Flytzani-Stephanopoulos, E.C.H. Sykes, Isolated Metal Atom

Geometries as a Strategy for Selective Heterogeneous Hydrogenations, Science 335 (2012) 1209, https://doi.org/10.1126/science.1215864.
[60] L.-W. Chen, X. Guo, R.-Y. Shao, Q.-Q. Yan, L.-L. Zhang, Q.-X. Li, H.-W. Liang, Structurally ordered intermetallic Ir_3V electrocatalysts for alkaline hydrogen evolution reaction, Nano Energy 81 (2021), https://doi.org/10.1016/j.nanoen.2020.105636 105636.
[61] H.Q. Fu, M. Zhou, P.F. Liu, P. Liu, H. Yin, K.Z. Sun, H.G. Yang, M. Al-Mamun, P. Hu, H.F. Wang, H. Zhao, Hydrogen Spillover-Bridged Volmer/Tafel Processes Enabling Ampere-Level Current Density Alkaline Hydrogen Evolution Reaction under Low Overpotential, J. Am. Chem. Soc. 144 (2022) 6028, https://doi.org/10.1021/jacs.2c01094.